

Asymmetric seafloor depth across the Juan de Fuca Ridge caused by lithospheric heating

Mengyu Wu¹   & Michael H. Ritzwoller¹

Previous studies attribute asymmetries across the East Pacific Rise to horizontal temperature or pressure gradients in the deep asthenosphere caused by the Pacific Superswell, which, however, cannot explain asymmetries observed across the Juan de Fuca Ridge. Here, we provide seismic evidence that the asymmetric seafloor depth across the Juan de Fuca Ridge is primarily caused by thermal buoyancy due to lithospheric heating and thinning. Based on a seismic model generated from Rayleigh wave measurements, we demonstrate that the seafloor depth on the western flank of the ridge, which is shallower (> 150 m) than the prediction from the plate age, agrees with the relatively younger apparent thermal age inferred from the seismic data, whereas the buoyancy of the deeper asthenosphere alone can only account for <25% of the rise. On the eastern flank, both plate age and apparent thermal age are consistent with observed seafloor depth.

¹Department of Physics, University of Colorado Boulder, Boulder, CO 80309, USA. ✉email: mewu4448@colorado.edu

The subsidence of the oceanic seafloor as a function of age has been demonstrated to vary approximately linearly with the square root of plate age up to 70–80 Ma^{1–4}, consistent with conductive cooling⁵. For ages between 0 and 70 Ma, the global average rate of seafloor subsidence, C_1 , has been estimated to be about 350 m Myr^{-1/2}². At older ages, this relationship breaks down, and the flattening of bathymetry with age has been attributed to reheating caused by processes such as small-scale mantle convection^{6–8}. This flattening can also be explained by a combination of other factors, such as secular cooling, as suggested in a recent model for the evolution of the oceanic lithosphere^{9, 10}.

For young plates near mid-ocean ridges, with ages up to around 10 Ma, seafloor subsidence rates typically range from 340 to 390 m Myr^{-1/2}¹¹. An anomalously low subsidence rate of 200–225 m Myr^{-1/2} has been observed on the western flank of the East Pacific Rise (EPR), in contrast to the normal rate of 350–400 m Myr^{-1/2} on its eastern flank¹¹. Seismic studies have revealed lower seismic velocity in the asthenosphere west of the EPR axis¹², indicating higher temperature (and/or more melt), lower density, and greater buoyancy, which are consistent with the observed elevated seafloor depth. Asymmetries observed across mid-ocean ridges have been investigated by various studies^{11, 13–19}. In particular, the asymmetric zone of the potential melt beneath the EPR has been explained by a horizontal pressure gradient that drives asthenospheric flow from hotspots in the Pacific Superswell region back to the EPR^{14, 15}, and the asymmetric seafloor depth across the EPR has been attributed to buoyancy resulting from a horizontal temperature gradient covering the top 150 km of the mantle¹¹ or a horizontal pressure gradient applied to the top 170 km¹⁵.

Similar to the East Pacific Rise, we observe that the seafloor depths are asymmetric across the Juan de Fuca (JdF) Ridge (Fig. 1a), with the depths on its western flank typically more than 150 m shallower than predicted using a subsidence rate C_1 of 350 m Myr^{-1/2} (Fig. 1b, c). In contrast, on the eastern flank, the seafloor depth is rarely more than 100 m shallower than the prediction after correcting for sediment thickness (see “Methods”), except for regions influenced by propagator wakes. Statistically, on the eastern flank of the JdF Ridge (Fig. 1d, e), bathymetry predicted from plate age is generally within one standard deviation of the observation. In contrast, on the western flank, the prediction is more consistent with a lower subsidence rate of 225 m Myr^{-1/2}, similar to the western flank of the East Pacific Rise. Moreover, seismic studies resulting from the recent Cascadia Initiative experiment²⁰ have also illustrated a hotter asthenosphere to the west of the JdF Ridge axis in the depth range of 30–60 km, inferred from a pronounced slow seismic velocity anomaly^{21–23}.

Although similar asymmetries are observed near the EPR and the JdF Ridge, the underlying physical mechanisms differ between the two regions. The horizontal pressure gradient that may explain the asymmetry in seafloor depth near the EPR is unlikely to exist near the JdF Ridge due to the lack of a superswell to the west of the ridge axis, as previous study has pointed out²¹. Other explanations based on thermal buoyancy in the asthenosphere, such as a constant horizontal temperature gradient covering hundreds of kilometers laterally¹¹ and an inflow temperature anomaly from thousands of kilometers west of the ridge axis¹⁵, are inconsistent with the location of the most likely source of the temperature anomaly, the Cobb Hotspot. It has been argued that the asymmetry of the melting region results from a modest horizontal gradient in temperature or composition occurring at the bottom boundary (100–120 km) of their model¹⁷, however the impact of this gradient on seafloor depth was not addressed.

In this study, we test the hypothesis that the observed seafloor depth asymmetry across the JdF Ridge is primarily caused by the thermal buoyancy at relatively shallower depths (< 30 km) in the

uppermost mantle, which contrasts with deeper asthenospheric buoyancy (i.e., at depths in 50–150 km) considered in previous studies^{11, 15}. We refer to this possibility as lithospheric heating, although it may also encompass a portion of the uppermost asthenosphere (20–30 km).

We do this through recently obtained seismic evidence, in which the lithospheric structure is characterized by its apparent thermal age (hereafter thermal age), which is the time it would take conductive cooling to generate the thermal structure inferred from the seismic data. Our thermal age estimate is taken from a published seismic model²³, which is produced by adopting a thermo-seismic hybrid parameterization in a Bayesian Markov Chain Monte Carlo (MCMC) seismic inversion using Rayleigh wave phase speed observations (Fig. 2, see “Methods” for details). Next, we compare the thermal age with the plate age estimated from magnetic anomalies²⁴ and the seafloor depth observation. Our results show that the apparent thermal age is notably younger than the plate age on the western flank of the JdF Ridge and the predicted seafloor depth from the thermal age agrees with the observed seafloor depth, which supports our hypothesis that the seafloor depth asymmetry across the JdF Ridge is primarily caused by thermal buoyancy at relatively shallow depths (< 30 km). Although the estimates of thermal age are limited within a region of up to 70–80 km to the west of the northern part of the JdF Ridge (Fig. 3b), the region is sufficient to test our hypothesis.

Results

Comparing ages: apparent thermal age and plate age. The apparent thermal age estimated near the Juan de Fuca Ridge (and across the JdF Plate) increases approximately linearly with distance from the ridge axis (Fig. 3a). Thermal age and plate age are largely consistent across the JdF Plate (Fig. 3b), with 68% of the area exhibiting a difference less than twice the uncertainty of the thermal age estimate (standard deviation of the posterior distribution of this estimate). Discrepancies near the subduction trench are discussed in a previous publication²³. Here, we focus on the region near the northern part of the JdF Ridge (Fig. 3b, within the red rectangle).

Our results reveal a clear asymmetry in the difference between the plate age and thermal age across the JdF Ridge. On the western flank of the ridge, thermal age estimates are younger than the plate age by greater than twice the thermal age uncertainty, as shown by the red to brown dots (Fig. 3b). In contrast, on the eastern flank, the two ages are largely consistent within the thermal age uncertainty, as shown by the white dots. A few black outliers exist close to the northwestern edge of our boxed region, which we exclude from further discussion because they may be caused by a lack of seismic station coverage.

The discrepancy between thermal age and plate age on the western flank of the JdF Ridge and their consistency on the eastern flank are evident from a statistical analysis of their variations with distance, at least up to 70 km from the ridge axis (Fig. 3c). The plate age is approximately symmetric across the ridge compared to the thermal age, reaching around 2.6 Ma at 70 km from the ridge on both sides. To make a statistical comparison between the plate age and thermal age, the uncertainties of both ages (shown as error bar in Fig. 3c) within each distance bin are estimated -- see “Methods”. For the plate age, the uncertainty varies between 0.3 and 0.6 Myr. In contrast, the thermal age is highly asymmetric across the ridge. On the eastern flank, thermal age follows a similar variation as plate age, increasing to ~2.5 Ma at 70 km from the ridge, but with larger uncertainties because it also involves the uncertainty from the seismic observations. On the western flank, the estimated thermal age is younger and remains around 0.5 Ma for distances <30 km

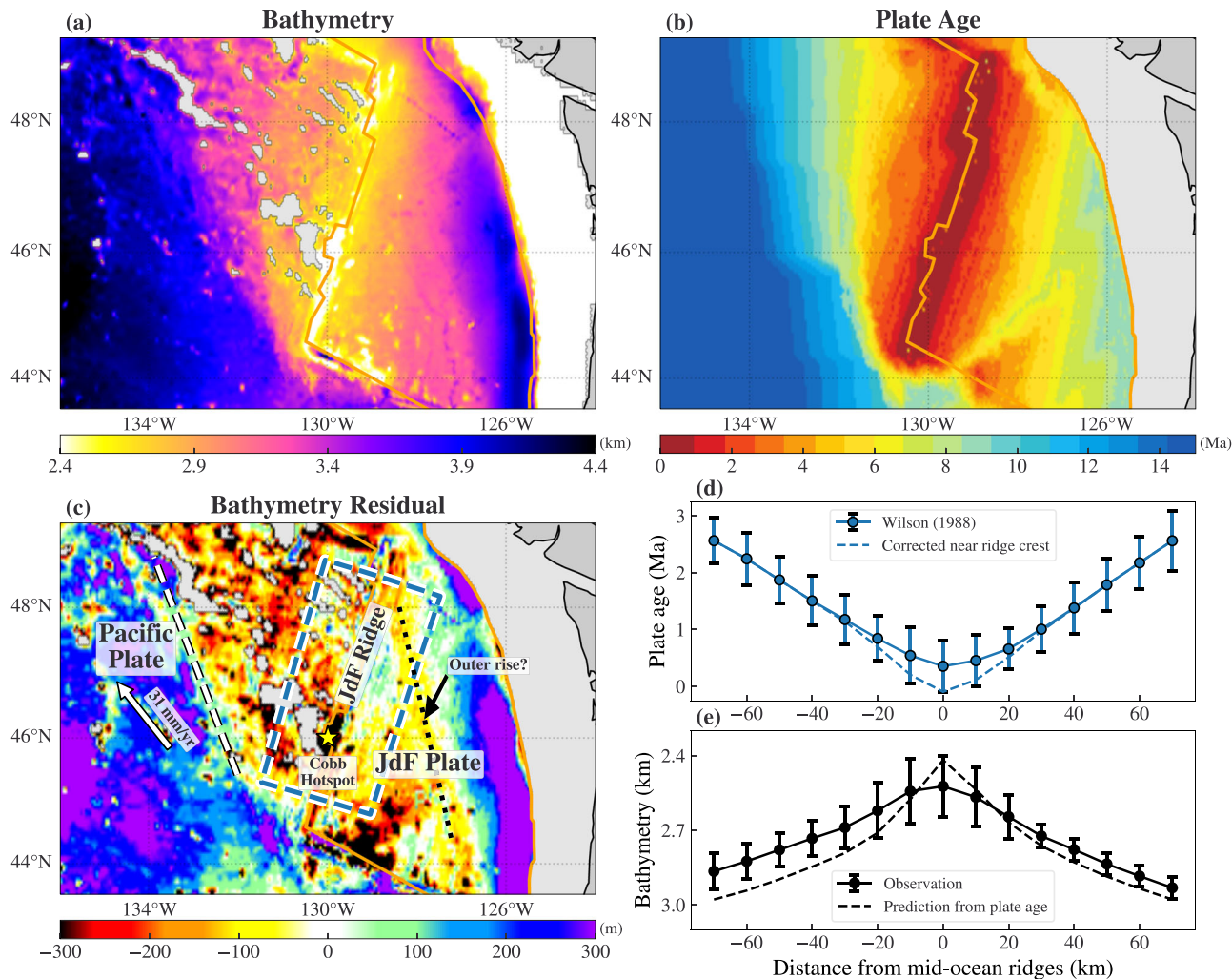


Fig. 1 Seafloor depth (bathymetry) asymmetry and the comparison between observation and prediction. **a** Asymmetric bathymetry across the JdF Ridge. The bathymetry is based on ETOPO2³⁴, and a sediment correction has been applied. Outliers of bathymetry west of the JdF Ridge have been eliminated (gray regions). Orange lines indicate plate boundaries. **b** Plate age is from previous regional study²⁴ where it exists and global model⁴⁸ otherwise. **c** Difference between the observed and predicted bathymetry, where yellow to red colors indicate that the observed bathymetry is shallower than the prediction from plate age assuming a subsidence rate C_1 of $350 \text{ m Myr}^{-1/2}$. Blue dashed box delineates the region used for **(d)** and **(e)**. White arrow shows the plate motion of the Pacific plate relative to the JdF Ridge. White dashed line indicates the boundary between the shallower and deeper bathymetry regions, which corresponds to one of the propagator wakes there. **d** Plate age with distance from the ridge. Solid blue curve with error bars shows the average and standard deviation within each 20 km width bin. The non-zero age at the ridge axis due to spatial averaging is corrected by applying a Gaussian-shape correction centered at the ridge axis with a sigma of 15 km, as shown by the dashed curve. **e** Black line with error bars shows the averages and standard deviations of the bathymetry observation within each 20 km width bin. Dashed line shows the prediction of bathymetry using the dashed curve in **(d)**, assuming a subsidence rate of $350 \text{ m Myr}^{-1/2}$.

from the ridge. This approximately constant thermal age as function of distance from the ridge on the western flank may be an artifact because the period range of surface wave observations used in this study ($>10 \text{ s}$) is not sensitive to thermal ages younger than 0.5 Ma due to the thinness of the lithosphere. Nevertheless, the thermal age is much younger than the plate age for this region. Starting at 40 km from the ridge on its western flank, the estimated thermal age increases with distance and reaches around 1 Ma at 70 km from the ridge. The difference between the plate age and thermal age is larger than the sum of their uncertainties on the western flank, suggesting a disagreement between these two ages west of the ridge.

Comparing seafloor depths: predictions and observation. We now compare observations of seafloor depth with predictions derived from two ages: the thermal age and the plate age. To

make the prediction, we use a half-space cooling model assuming isostatic equilibrium has been reached by 150 km depth and present predictions for a range of seafloor depths, accounting for the uncertainty in both thermal and plate ages and the cooling model variables (Fig. 4a), see “Methods”. The predictions of seafloor depth derived from the plate age and thermal age are displayed as blue and orange shaded areas, respectively, with the mean and the standard deviation of the observed seafloor depth in each distance bin shown as black bars (Fig. 4b). We exclude predictions within 20 km of the ridge axis, as the ages are over-estimated when averaging within bins close to the ridge axis.

On the western flank of the ridge, the average seafloor depth increases from 2663 m at 20 km to 2872 m at 70 km from the ridge axis, with spatial standard deviations of around 65 m. The predicted seafloor depth from the plate age is deeper than the observation, with the upper limit of the prediction envelope being, on average, 130 m deeper than the mean of the

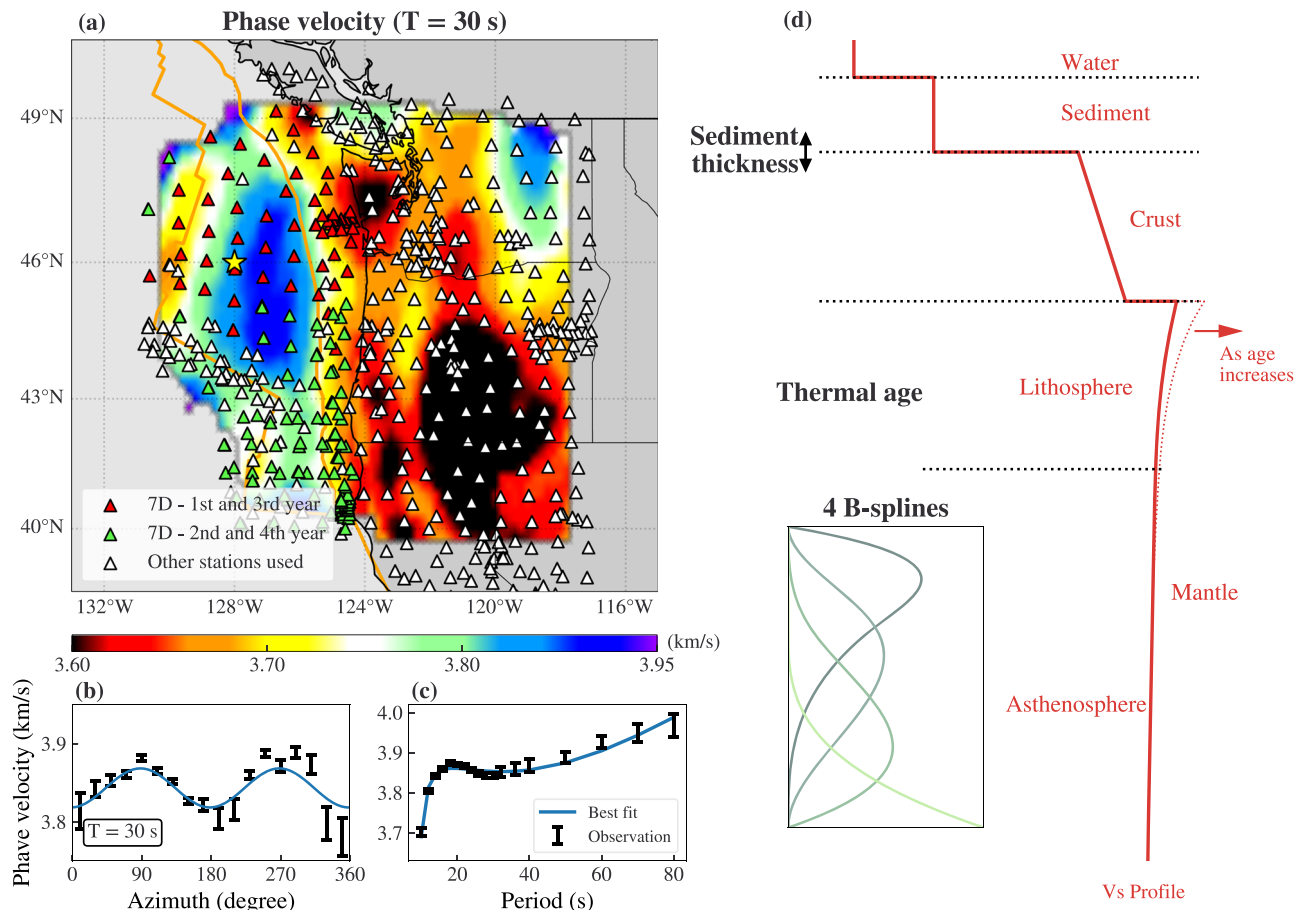


Fig. 2 Estimating apparent thermal age with a Bayesian MCMC inversion of Rayleigh wave phase speed data. **a** Rayleigh wave phase speed map at 30 s period. Triangles represent the seismic stations used in generating the Rayleigh wave phase speed dataset³⁵. Red and green triangles are stations of network 7D (the main component of the Cascadia Initiative experiment) deployed asynchronously. Star indicates the location of the example point of **(b)** and **(c)**. **b** An example of phase speed variation with azimuth (ψ). Error bars show the estimated uncertainties and blue line is the best fit of the $2\text{-}\psi$ variation that is removed before inversion. **c** Rayleigh wave isotropic phase speed with period. Error bars show the estimated uncertainties and blue line is the prediction of phase speed from the mean model of the posterior distribution from the MCMC inversion. **d** Illustration of the model parameterization, modified from a previous publication²³. Bold black text indicates the six model variables that are estimated during inversion.

observation. This discrepancy is twice the standard deviation of the observations. In contrast, the prediction envelope from the thermal age encompasses the means of the observations, including the error bars. Therefore, on the western flank of the Juan de Fuca Ridge, these predictions indicate that the thermal age matches the seafloor depth, but the plate age does not.

On the eastern flank, predictions from the plate age and thermal age are consistent with one another, although the range of predictions from thermal age is larger than from the plate age, and both match with the observed seafloor depth. The upper limit of the prediction envelope from thermal age roughly corresponds to the mean of the observation, which ranges from 2681 m at 20 km to 2952 m at 70 km. The upper limit of the prediction envelope derived from the plate age is slightly deeper but still broadly consistent with the observed seafloor depth within one standard deviation (~ 48 m). The match of observations and predictions lie near the edges of the prediction envelopes, which may be caused by the involvement of effects other than lithospheric thermal structure, such as the bending of the JdF Plate due to its subduction beneath North America. A possible sign of the rise of the seafloor due to bending, i.e., the outer rise, is apparent after subtracting the subsidence with age (Fig. 1a, dotted black line). Nevertheless, we consider the seafloor depth to be consistent with both the thermal age and plate age on the eastern flank of the JdF Ridge.

Discussion

Our results show that the estimated apparent thermal age near the Juan de Fuca Ridge is notably younger than the plate age on the ridge's western flank. As the thermal age is not the real age of the plate but a measure of its lithospheric thermal structure, the young thermal age implies that lithospheric thermal structure is warmer than what would be predicted based on the plate age. This leads to greater thermal expansion, more buoyancy, and less subsidence of the seafloor, which is qualitatively consistent with observations of seafloor depth. On the eastern flank of the ridge, our estimated thermal age is consistent with the plate age and the conductive cooling model, at least at plate ages <3 Ma.

Quantitative comparisons between observed and predicted seafloor depths show that the seafloor depth prediction derived from the thermal age is consistent with observations on both flanks of the ridge. This agreement indicates that the thermal structure of the lithosphere primarily determines seafloor depth, and, on the western flank of the JdF Ridge the hotter and thinner lithosphere is enough to explain the observed elevated seafloor depth. Conversely, the prediction from the plate age only agrees with the observed seafloor depth on the eastern flank of the ridge. On the western flank, the lithospheric temperature predicted from the plate age is too low to explain the observed shallow seafloor depth, even when considering a weaker cooling effect than the global average.

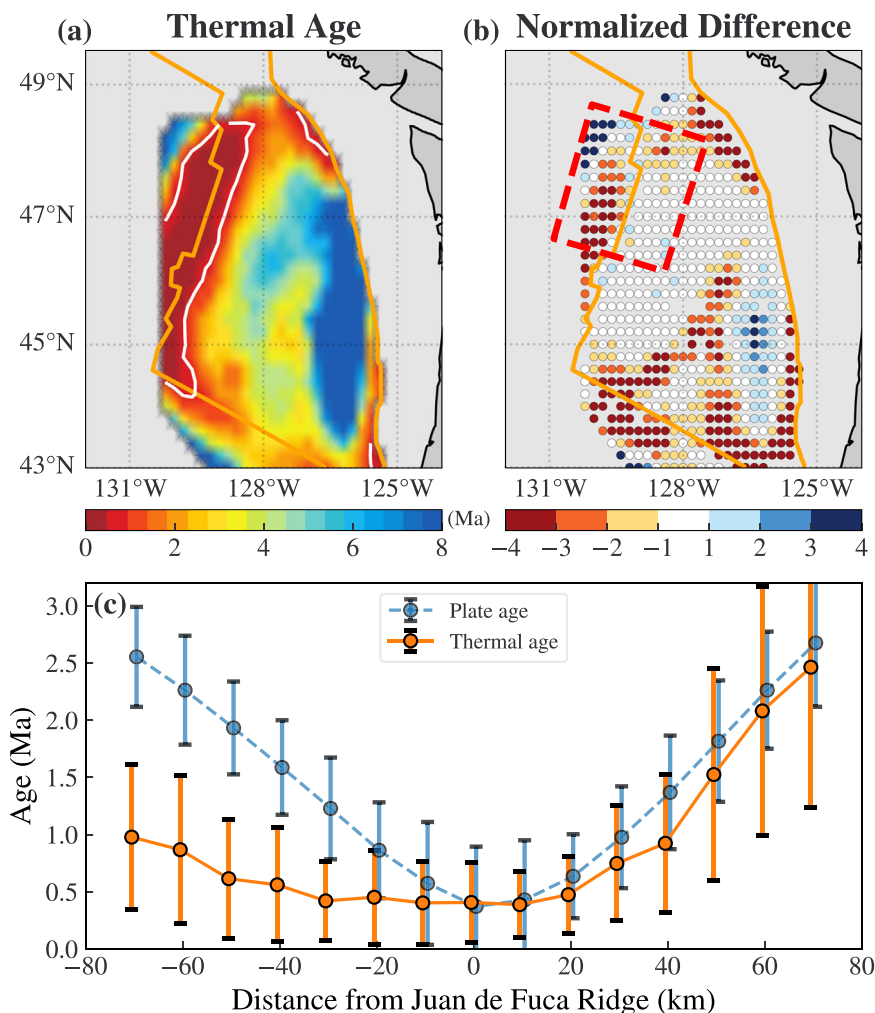


Fig. 3 Estimated apparent thermal age and comparison with the plate age. **a** Apparent thermal age estimated from the MCMC inversion. White lines are the 1 Ma contours. **b** Thermal age minus plate age, normalized by thermal age uncertainty. Warm colors mean the thermal age is younger than the plate age and the lithosphere is hotter than expected. Cool colors mean the thermal age is older than the plate age and a colder lithosphere is expected. Red dashed rectangle delineates the region used in **(c)**. **c** Variations of the plate age and thermal age with distance across the northern part of the JdF Ridge. Error bars are the estimated uncertainties in each bin, see “Methods” for details. The longer thermal age error bars to the east of the JdF Ridge than to the west is due to the less sensitivity of surface wave observation to the change of thermal age as age increases.

The observed asymmetry of a hotter lithosphere to the west of the JdF Ridge compared to a plate-age-consistent lithosphere to the east of the ridge implies that the uppermost asthenosphere (e.g., at depths < 30 km) on the western flank remains hot as it ages, which results in a hotter and thinner lithosphere than predicted from the plate age. The mechanism responsible for creating the thermal anomaly at such a shallow depth remains unclear. The asymmetric mantle upwelling beneath the Juan de Fuca ridge triggered by the Cobb Hotspot, as suggested by previous study²¹, may offer the required warmer environment for the lithospheric and uppermost asthenospheric heating. Better understanding would require geodynamic modeling.

Thermal buoyancy in the asthenosphere at greater depths (> 30 km) is another potential factor to explain the observed seafloor depth residual. However, estimating the contribution of this effect is more challenging due to the considerable uncertainty of the temperature and thermal expansion coefficient in the asthenosphere, particularly at young ages where partial melt may occur. Here, we assume that the buoyancy due to small amounts of melt is negligible and consider only the mantle thermal expansion in the asthenosphere based on an isostatic calculation.

To investigate the potential contribution of the asthenosphere to the observed shallower seafloor depths, we estimate the temperature variation in the asthenosphere using shear wave speeds averaged between 30 and 150 km depth in our published seismic model²³, and calculate its effect on seafloor depth assuming that isostatic equilibrium is reached by 150 km depth. Using a near-solidus dT/dV_S of $0.5 K m^{-1}$ ²⁵, where T is the temperature and V_S is the seismic shear velocity, and a moderate thermal expansion coefficient of $\alpha = 3.2 \times 10^{-5} K^{-1}$, we find a maximum 70 m uplift of seafloor depth at around 45 km to the west of the JdF Ridge axis (Fig. 5b). This effect is small compared with the observed seafloor depth deviation (Fig. 5c, left part). Increasing the temperature variation or thermal expansion coefficient would help explain the shallow seafloor depth on the western flank, but it would lead to unrealistic greater depths on the eastern flank (Fig. 5c, right part). In addition, the distance trend of the average V_S (and the predicted effect on seafloor depth) follows a “U” shape (Fig. 5a, b), which is inconsistent with the approximately flat trend observed in the seafloor depth residual (Fig. 1c). Therefore, we suggest the asthenospheric effect to be secondary to the lithospheric thermal variation near the JdF Ridge, in contrast to the East Pacific

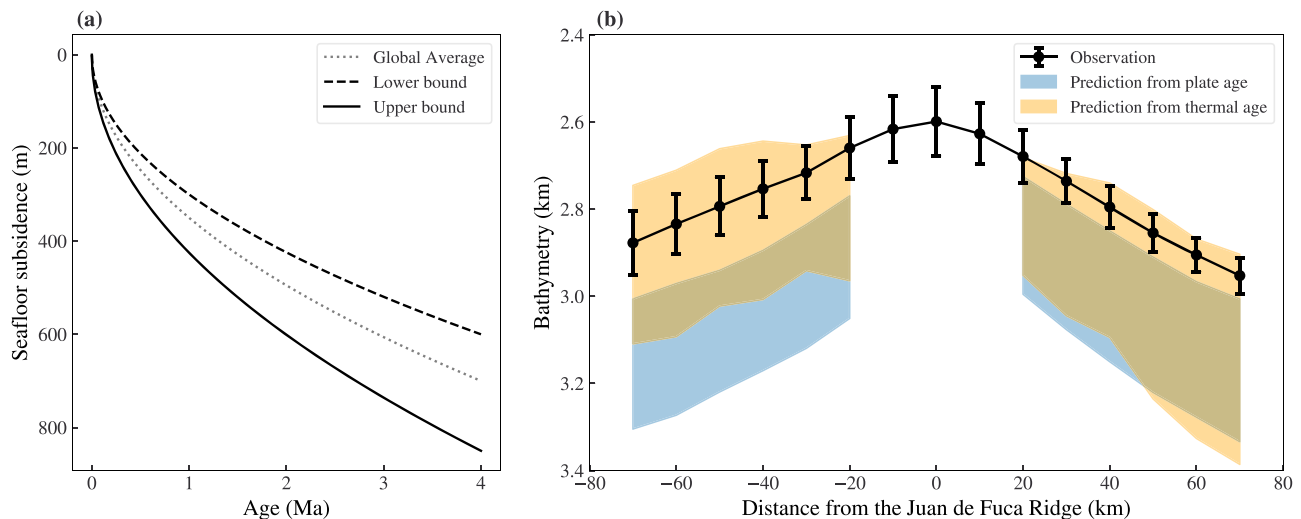


Fig. 4 Comparison between seafloor depth predictions and observation. **a** Seafloor depth prediction with different subsidence coefficients C_1 . Global average = $350 \text{ m Myr}^{-1/2}$, lower bound = $300 \text{ m Myr}^{-1/2}$, upper bound = $425 \text{ m Myr}^{-1/2}$. **b** Seafloor depth prediction and observation near the northern part of the JdF Ridge. Blue and yellow shaded areas represent predictions from the plate and thermal age, respectively. The mean and standard deviation of seafloor depth observation within each distance bin is shown with black error bars.

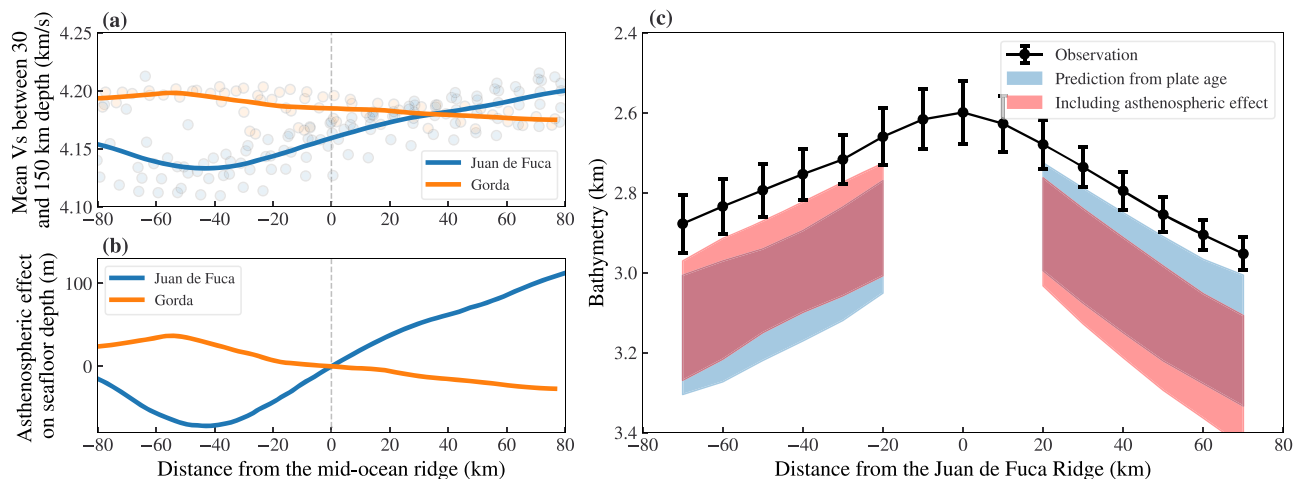


Fig. 5 Effect of asthenospheric buoyancy estimated from seismic shear wave velocity. **a** Average shear wave speed between 30 and 150 km depth. The scattered dots show the averaged speeds across the grid of our model, and their mean value with distance is shown by the solid line. **b** Estimated influence on the seafloor depth due to asthenospheric buoyancy, calculated from the solid curves in (a). In (a) and (b), the blue curve is for regions near the Juan de Fuca Ridge and the orange curve is near the Gorda Ridge. **c** Seafloor depth prediction with only asthenospheric buoyancy considered, assuming the lithospheric structure is consistent with the plate age, error bars showing the standard deviation within each distance bin.

Rise, where the seafloor elevation effect of asthenospheric buoyancy was estimated to be around 10 times larger than that of the lithospheric thermal expansion¹¹.

Factors other than temperature, such as crustal underplating and mantle depletion, can also generate buoyancy forces, but they are inconsistent with the seismic observations. Previous studies^{26, 27} have shown that the topography high of seamounts west of the EPR is due to crustal underplating (thickening). But the thickening of the crust will only lower the seismic Rayleigh wave phase speed at periods below 12 s and, therefore, cannot explain the observed slow seismic Rayleigh wave speeds at 16–30 s period. The greater degree of melting west of the JdF Ridge relative to the east may result in greater depletion and lower density of the uppermost mantle there. However, it has little effect on seismic velocity at shallow depths ($\sim 30 \text{ km}$)²⁸, which also disagrees with the observed slow seismic Rayleigh wave speeds mentioned above.

We also estimate thermal age near the Gorda Ridge, where no asymmetry is observed in seafloor depth or seismic

structure^{21–23, 29, 30}, and across the Gorda plate. Our estimated thermal age increases approximately linearly with distance on both sides of the ridge axis and decreases near the trench (Fig. 6a), similar to what is observed in the near-trench Juan de Fuca plate. Near the Gorda Ridge, the thermal age is slightly younger than the plate age, but there is no notable discrepancy except some outliers near the southern edge of the plate (Fig. 6b). A statistical comparison (Fig. 6c) confirms that the differences between the two ages are not larger than the sum of their uncertainties, indicating that the lithospheric thermal structure on both sides of the Gorda Ridge is not far from the prediction of the conductive cooling model.

After excluding regions affected by the central rift valley along the Gorda Ridge (within about 25 km from the axis), the seafloor depth predicted from the thermal age is consistent with the observation (Fig. 6d), confirming the lithospheric thermal structure is the primary factor in determining seafloor subsidence here, as well. The prediction from the plate age is

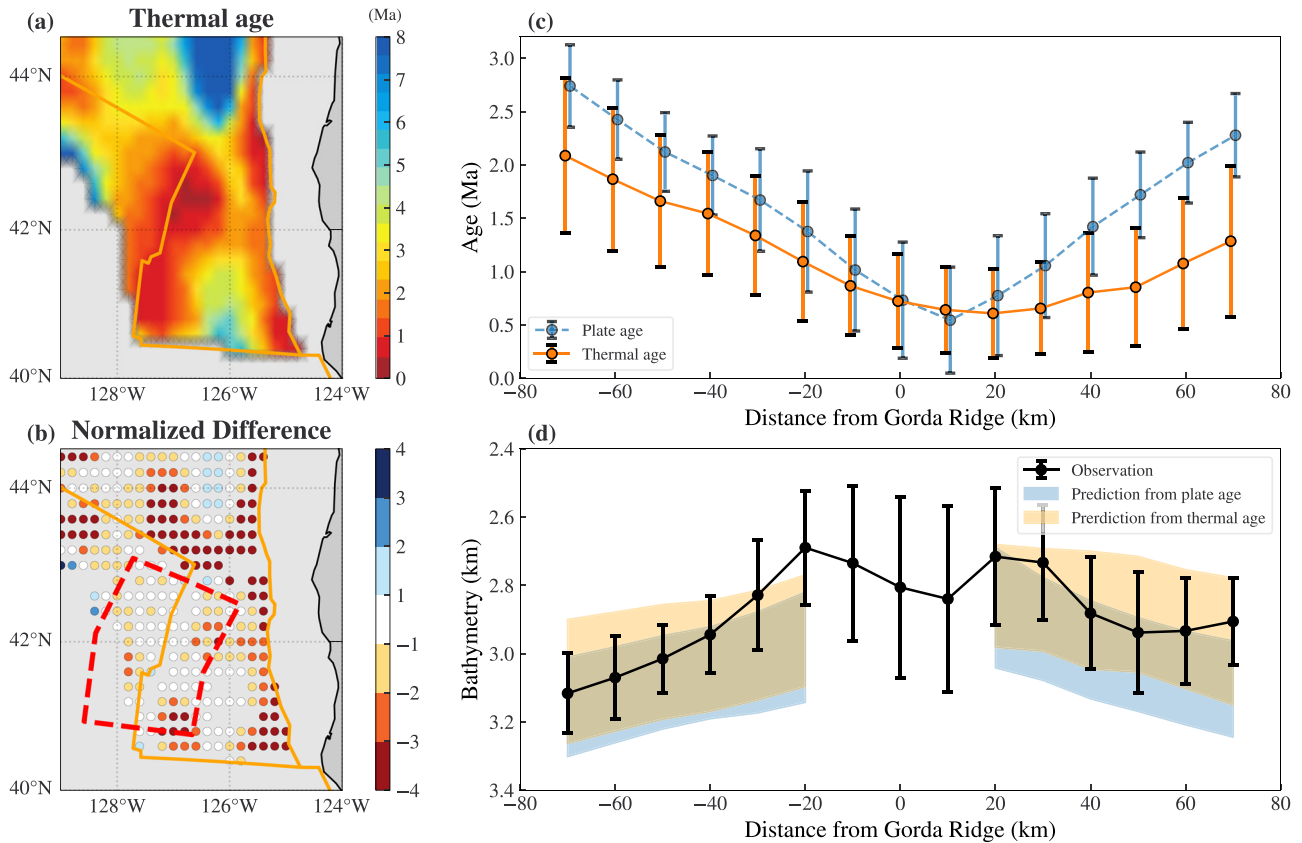


Fig. 6 Comparison of the plate age, thermal age, and seafloor depth near the Gorda Ridge. **a** Mean of the posterior distribution of the thermal age estimated from the MCMC inversion, focused on the Gorda Plate, similar to Fig. 3a. **b** Normalized difference between the thermal age and plate age, similar to Fig. 3b. Red dashed polygon delineates the region used in (c) and (d). **c** The variation of the plate age and thermal age across the Gorda Ridge, similar to Fig. 3c. **d** Comparison of the seafloor depth predictions of the plate age and thermal age, and the observations, similar to Fig. 4b.

deeper than that of the thermal age on average but is still within one standard deviation of the seafloor depth observation. The consistency of thermal age, plate age and seafloor depth suggests that the conductive cooling model is a good approximation in describing the evolution of the plate originating from the Gorda Ridge.

Methods

Sediment correction. Near the Juan de Fuca Ridge, the sediment thickness increases rapidly with distance from the ridge axis on the eastern flank and reaches 250 m at 50–70 km from the ridge³¹. No such rapid thickening of sediment is observed on the western flank. The relatively large accumulation of sediments and its asymmetry across the ridge makes it necessary to correct seafloor depth for sediment thickness. Here, we only consider the impact of sediment on isostatic equilibrium and ignore the insulation it provides on lithospheric cooling, as the sediment is much thinner than the lithosphere in most of the study region. Similar to previous studies^{32, 33}, seafloor depth w corrected for sediment thickness is calculated by:

$$w = w_{raw} + \left(\frac{\rho_m - \rho_s}{\rho_m - \rho_w} \right) h_s, \quad (1)$$

where w_{raw} is the raw observed seafloor depth, ρ_m , ρ_s and ρ_w are densities of the mantle, the sediment, and the seawater, respectively, and h_s is the sediment thickness. Here, we fix $\rho_w = 1.03 \times 10^3 \text{ kg m}^{-3}$, $\rho_m = 3.2 \times 10^3 \text{ kg m}^{-3}$ and $\rho_s = 1.65 \times 10^3 \text{ kg m}^{-3}$, which yields the correction coefficient in parentheses preceding h_s of around 0.7. We employ the bathymetry

of ETOPO2³⁴ as the raw seafloor depth, and the sediment thickness is from a global model³¹.

Rayleigh wave phase speed dataset. A Rayleigh wave phase speed dataset³⁵ is used to construct the thermal age estimates. This dataset is composed of Rayleigh wave measurements from earthquakes, the traditional two-station ambient noise method and a recently developed three-station ambient noise interferometry method. The original seismic recordings, primarily come from Cascadia Initiative experiment²⁰ offshore and USArray Transportable Array onshore (Fig. 2a), span from 2005 to 2015. Eikonal tomography³⁶ is applied to estimate the phase speed on a 0.2-by-0.2-degree grid for periods in the range of 10–40 s. For longer periods up to 80 s, Helmholtz tomography³⁷ is employed to account for finite frequency effects, which is more essential at longer periods. Examples of an estimated phase speed map as well as the azimuthal variation and dispersion of Rayleigh wave phase speeds are shown here (Fig. 2a–c). We only interpret the isotropic part of this dataset in this paper, which, however, is corrected for azimuthal anisotropy. We estimate the apparent thermal age to the west of the subduction trench, covering most of the Juan de Fuca and Gorda plates and including part of the Pacific plate adjacent to the Juan de Fuca Ridge, the Blanco Transform Fault, and the Gorda Ridge.

Bayesian MCMC inversion with thermo-seismic hybrid parameterization. The seismic model we use here is presented in a previous publication²³. The posterior distributions of model variables are estimated using a Bayesian Markov Chain Monte Carlo (MCMC) inversion method^{38–40}, which modifies the prior

information via the Metropolis-Hastings algorithm to generate a posterior distribution consistent with the Rayleigh wave phase speed observations. The thermal age estimate is derived as the mean of this posterior distribution, with the standard deviation denoting the associated uncertainty.

The resulting seismic model is constructed on a 0.2-by-0.2-degree grid. At each grid point, the model comprises four layers: water, sediment, crust, and mantle and constructed by six model variables: sediment thickness, thermal age of the lithosphere, and four B-spline coefficients of the seismic shear wave speed (V_S) in the asthenosphere. The sedimentary V_S is estimated from its thickness using an empirical relation⁴¹. The crustal layer is fixed at a constant thickness of 7 km, and its V_S is assumed to increase linearly with depth from 3.25 to 3.94 km s^{-1} ⁴² for thermal ages older than 4 Ma. For thermal ages younger than 4 Ma, a thermal expansion correction is applied to crustal V_S . During the inversion process, V_S is reconstructed directly from the model variables, whereas other variables required by the forward code⁴³ are derived thereafter. The speed of the seismic P wave (V_P) and the density (ρ) are derived from V_S using empirical relations^{44, 45}. The bulk attenuation factor (Q_κ) is set to be infinity and the shear attenuation factor (Q_μ) is assumed to be age-dependent, following the model estimated from fundamental Rayleigh wave⁴⁶.

This model adopts a thermo-seismic hybrid parameterization that divides the mantle into a lithospheric and an asthenospheric part, parameterizing these differently (Fig. 2d). In the lithosphere, the seismic structure is derived from the thermal age by converting the age-dependent thermal structure (consistent with a half-space cooling model) to V_S , similar to the thermal parameterization⁸. In this approach, a conductive cooling assumption is introduced as a physical constraint to reduce the null space in the inversion. Vertical structure perturbations inconsistent with conductive cooling will not be resulted in our inversion, but their vertically averaged effect will be reflected in the apparent thermal age. In the underlying asthenosphere, a traditional seismic parameterization is employed, which describes the seismic structure with four cubic B-splines for V_S . This reversion to the traditional parameterization below the lithosphere is due to the lack of a well-accepted conversion relation from temperature to V_S for the asthenosphere beneath a young plate, where the temperature could be high and close to the solidus. The interface between the lithosphere and the asthenosphere is thermal-age-dependent, defined as the depth where the predicted temperature reaches 92% of the solidus. Above this temperature, the anelasticity increases dramatically with temperature²⁵.

Seafloor depth prediction from age (thermal or plate). We assume that seafloor subsidence is mainly a consequence of the buoyancy variation caused by lithospheric conductive cooling (although the cooling time might be different from the plate age) with isostatic equilibrium in the upper mantle. For oceanic lithosphere younger than 10 Ma, the half-space cooling model and other models, such as the plate model², give similar seafloor depths. We compute seafloor depth from the half-space cooling model:⁴⁷

$$w(t) = w_0 + C_1 \sqrt{t}, \quad (2)$$

$$C_1 = \frac{2\rho_m \alpha (T_m - T_s)}{\rho_m - \rho_w} \left(\frac{\kappa}{\pi} \right)^{\frac{1}{2}}. \quad (3)$$

Here, $w(t)$ is the seafloor depth as a function of age in Ma, w_0 is the seafloor depth at the ridge crest, C_1 is the subsidence rate with age, ρ_m is the density of mantle, ρ_w is the density of seawater, $T_m - T_s$ is the temperature difference between the mantle and the seafloor surface, α is the coefficient of thermal expansion, κ is the thermal

diffusivity, and t is the lithospheric age (either the plate or thermal age in this study, in Ma). The apparent thermal age is obtained through Bayesian MCMC inversion mentioned above and the plate age is taken from a regional model²⁴ and supplemented by a global plate age model⁴⁸. To match the resolution of the thermal age (around 70–80 km), a Gaussian smoothing filter with a sigma of 15 km is applied to the plate age before use.

For regions near the Juan de Fuca Ridge, w_0 is estimated as the average of the seafloor depth within 5 km of the ridge axis, which is 2418 m averaged over the whole JdF Ridge and 2567 m for its northern part alone. However, this approach is not feasible for regions near the Gorda Ridge due to the presence of a deep median valley along the axis of the Gorda spreading center. Thus, we manually picked $w_0 = 2,550 \text{ m}$ for the Gorda Ridge by extrapolating seafloor depths with distance from the spreading center larger than 25 km back to the spreading center.

To estimate the uncertainties of age and the coefficient C_1 preceding \sqrt{t} in Eq. (2), we calculated the upper/lower bound of seafloor depth from the upper/lower bounds of age and C_1 . The bounds of ages are taken from the error bar of each distance bin (Fig. 3c); i.e., one uncertainty above and below the average. For plate age, the uncertainty here is estimated as the spatial standard deviation within each distance bin. For thermal age, this involves both the spatial standard deviation and the average of individual thermal age uncertainties within each distance bin, computed as the square root of the sum of their squares. Individual thermal age uncertainty is the standard deviation of the posterior distribution of thermal age obtained in the Bayesian MCMC inversion. The value of C_1 varies in different studies and study areas. Global studies suggest it is 350 $\text{m Myr}^{-1/2}$, on average, for plates younger than 70 Ma² and 340–390 $\text{m Myr}^{-1/2}$ near mid-ocean ridges¹¹. To reflect the potential variation, we choose a wide range of C_1 with an upper bound of 425 $\text{m Myr}^{-1/2}$, corresponding to $\rho_m = 3.2 \times 10^3 \text{ kg m}^{-3}$, $\alpha = 3.4 \times 10^{-5} \text{ K}^{-1}$, $T_m - T_s = 1,350 \text{ K}$ and $\kappa = 1.0 \times 10^{-6} \text{ m}^2 \text{ s}^{-1}$, and a lower bound of 300 $\text{m Myr}^{-1/2}$, corresponding to $\rho_m = 3.4 \times 10^3 \text{ kg m}^{-3}$, $\alpha = 3.0 \times 10^{-5} \text{ K}^{-1}$, $T_m - T_s = 1,250 \text{ K}$ and $\kappa = 0.8 \times 10^{-6} \text{ m}^2 \text{ s}^{-1}$ (Fig. 4a).

Data availability

Broadband seismic waveforms are retrieved from IRIS-DMC (<https://ds.iris.edu/ds/nodes/dmc/>). Rayleigh wave phase speed dataset, the estimated thermal age with uncertainty, and the 3D seismic model compiled from means of the posterior distribution of model variables used/obtained in this study are available in Zenodo under <https://doi.org/10.5281/zenodo.7806857>.

Code availability

The python packages and codes in running MCMC inversion, predicting seafloor depths and making all figures are available in Zenodo under <https://doi.org/10.5281/zenodo.7806913> or upon request from corresponding authors.

Received: 10 May 2023; Accepted: 26 October 2023;

Published online: 04 November 2023

References

1. Parker, R. L. & Oldenburg, D. W. Thermal model of ocean ridges. *Nat. Phys. Sci.* **242**, 137–139 (1973).
2. Parsons, B. & Sclater, J. G. An analysis of the variation of ocean floor bathymetry and heat flow with age. *J. Geophys. Res.* **82**, 803–827 (1977).
3. Stein, C. A. & Stein, S. A model for the global variation in oceanic depth and heat flow with lithospheric age. *Nature* **359**, 123–129 (1992).
4. Crosby, A. G., McKenzie, D. & Sclater, J. G. The relationship between depth, age and gravity in the oceans. *Geophys. J. Int.* **166**, 553–573 (2006).
5. Davis, E. E. & Lister, C. R. B. Fundamentals of ridge crest topography. *Earth Planetary Sci. Lett.* **21**, 405–413 (1974).

6. Parsons, B. & McKenzie, D. Mantle convection and the thermal structure of the plates. *J. Geophys. Res.* **83**, 4485 (1978).
7. Davaille, A. & Jaupart, C. Onset of thermal convection in fluids with temperature-dependent viscosity: Application to the oceanic mantle. *J. Geophys. Res. Solid Earth* **99**, 19853–19866 (1994).
8. Ritzwoller, M. H., Shapiro, N. M. & Zhong, S.-J. Cooling history of the Pacific lithosphere. *Earth Planetary Sci. Lett.* **226**, 69–84 (2004).
9. Korenaga, T. & Korenaga, J. Evolution of young oceanic lithosphere and the meaning of seafloor subsidence rate. *J. Geophys. Res.: Solid Earth* **121**, 6315–6332 (2016).
10. Korenaga, T., Korenaga, J., Kawakatsu, H., & Yamano, M. A New Reference Model for the Evolution of Oceanic Lithosphere in a Cooling Earth. *J. Geophys. Res.: Solid Earth*, **126**, <https://doi.org/10.1029/2020jb021528> (2021).
11. Cochran, J. R. Variations in subsidence rates along intermediate and fast spreading mid-ocean ridges. *Geophys. J. Royal Astronom. Soc.* **87**, 421–454 (1986).
12. The MELT Seismic Team. Imaging the deep seismic structure beneath a mid-ocean ridge: The MELT experiment. *Science* **280**, 1215–1218 (1998).
13. Eberle, M. A. & Forsyth, D. W. An alternative, dynamic model of the axial topographic high at fast spreading ridges. *J. Geophys. Res.: Solid Earth* **103**, 12309–12320 (1998).
14. Conder, J. A., Forsyth, D. W. & Parmentier, E. M. Asthenospheric flow and asymmetry of the East Pacific Rise, MELT area. *J. Geophys. Res.: Solid Earth* **107**, ETG 8–1–ETG 8–13 (2002).
15. Toomey, D. R. et al. Asymmetric mantle dynamics in the MELT region of the East Pacific Rise. *Earth Planetary Sci. Lett.* **200**, 287–295 (2002).
16. Katz, R. F., Spiegelman, M., & Carbotte, S. M. Ridge migration, asthenospheric flow and the origin of magmatic segmentation in the global mid-ocean ridge system. *Geophys. Res. Lett.* **31** <https://doi.org/10.1029/2004gl020388> (2004)
17. Katz, R. F. Porosity-driven convection and asymmetry beneath mid-ocean ridges. *Geochem. Geophys. Geosyst.* **11**, <https://doi.org/10.1029/2010gc003282> (2010).
18. Watkins, C. E. & Conrad, C. P. Constraints on dynamic topography from asymmetric subsidence of the mid-ocean ridges. *Earth Planetary Sci. Lett.* **484**, 264–275 (2018).
19. Pusok, A. E., Katz, R. F., May, D. A. & Li, Y. Chemical heterogeneity, convection and asymmetry beneath mid-ocean ridges. *Geophys. J. Int.* **231**, 2055–2078 (2022).
20. Toomey, D. et al. The Cascadia Initiative: A sea change in seismological studies of subduction zones. *Oceanography* **27**, 138–150 (2014).
21. Bell, S., Ruan, Y. & Forsyth, D. W. Ridge asymmetry and deep aqueous alteration at the trench observed from Rayleigh wave tomography of the Juan de Fuca plate. *J. Geophys. Res. Solid Earth* **121**, 7298–7321 (2016).
22. Byrnes, J. S., Toomey, D. R., Hooft, E. E. E., Nábělek, J. & Braunmiller, J. Mantle dynamics beneath the discrete and diffuse plate boundaries of the Juan de Fuca plate: Results from Cascadia Initiative body wave tomography. *Geochem. Geophys. Geosyst.* **18**, 2906–2929 (2017).
23. Wu, M., Wang, H., Zhang, S., & Ritzwoller, M. H. Plate Age and Uppermost Mantle Structure Across the Juan de Fuca and Gorda Plates. *J. Geophys. Res.: Solid Earth* **128**, <https://doi.org/10.1029/2023jb026494> (2023)
24. Wilson, D. S. Tectonic history of the Juan de Fuca Ridge over the last 40 million years. *J. Geophys. Res. Solid Earth* **93**, 11863–11876 (1988).
25. Yamauchi, H. & Takei, Y. Polycrystal anelasticity at near-solidus temperatures. *J. Geophys. Res. Solid Earth* **121**, 7790–7820 (2016).
26. Harmon, N., Forsyth, D. W., & Scheirer, D. S. Analysis of gravity and topography in the GLIMPSE study region: Isostatic compensation and uplift of the Sojourn and Hotu Matua Ridge systems. *J. Geophys. Res.: Solid Earth*, **111**, <https://doi.org/10.1029/2005jb004071> (2006).
27. Harmon, N., Forsyth, D. W., Weeraratne, D. S., Yang, Y. & Webb, S. C. Mantle heterogeneity and off axis volcanism on young Pacific lithosphere. *Earth Planetary Sci. Lett.* **311**, 306–315 (2011).
28. Schutt, D. L., & Leshner, C. E. Effects of melt depletion on the density and seismic velocity of garnet and spinel lherzolite. *J. Geophys. Res. Solid Earth* **111**, <https://doi.org/10.1029/2003jb002950> (2006).
29. Eilon, Z. C. & Abers, G. A. High seismic attenuation at a mid-ocean ridge reveals the distribution of deep melt. *Sci. Adv.* **3**, e1602829 (2017).
30. Rychert, C. A., Harmon, N. & Tharimena, S. Scattered wave imaging of the oceanic plate in Cascadia. *Sci. Adv.* **4**, ea01908 (2018).
31. Whittaker, J. M., Goncharov, A., Williams, S. E., Müller, R. D. & Leitchenkov, G. Global sediment thickness data set updated for the Australian–Antarctic Southern Ocean. *Geochem. Geophys. Geosyst.* **14**, 3297–3305 (2013).
32. Sykes, T. J. S. A correction for sediment load upon the ocean floor: Uniform versus varying sediment density estimations—implications for isostatic correction. *Marine Geol.* **133**, 35–49 (1996).
33. Adam, C., & Bonneville, A. Extent of the South Pacific Superswell. *J. Geophys. Res.: Solid Earth* **110**, <https://doi.org/10.1029/2004jb003465> (2005)
34. Smith, W. H. F. & Sandwell, D. T. Global sea floor topography from satellite altimetry and ship depth soundings. *Science* **277**, 1956–1962 (1997).
35. Zhang, S., Wang, H., Wu, M. & Ritzwoller, M. H. Isotropic and azimuthally anisotropic Rayleigh wave dispersion across the Juan de Fuca and Gorda plates and U.S. Cascadia from earthquake data and ambient noise two- and three-station interferometry. *Geophys. J. Int.* **226**, 862–883 (2021).
36. Lin, F., Ritzwoller, M. H. & Snieder, R. Eikonal tomography: surface wave tomography by phase front tracking across a regional broad-band seismic array. *Geophys. J. Int.* **177**, 1091–1110 (2009).
37. Lin, F. & Ritzwoller, M. H. Helmholtz surface wave tomography for isotropic and azimuthally anisotropic structure. *Geophys. J. Int.* **186**, 1104–1120 (2011).
38. Shen, W., Ritzwoller, M. H., Schulte-Pelkum, V. & Lin, F.-C. Joint inversion of surface wave dispersion and receiver functions: a Bayesian Monte-Carlo approach. *Geophys. J. Int.* **192**, 807–836 (2013).
39. Shen, W. & Ritzwoller, M. H. Crustal and uppermost mantle structure beneath the United States. *J. Geophys. Res. Solid Earth* **121**, 4306–4342 (2016).
40. Feng, L. & Ritzwoller, M. H. A 3-D shear velocity model of the crust and uppermost mantle beneath Alaska including apparent radial anisotropy. *J. Geophys. Res.: Solid Earth* **124**, 10468–10497 (2019).
41. Ruan, Y., Forsyth, D. W. & Bell, S. W. Marine sediment shear velocity structure from the ratio of displacement to pressure of Rayleigh waves at seafloor. *J. Geophys. Res.: Solid Earth* **119**, 6357–6371 (2014).
42. Tian, Y., Shen, W. & Ritzwoller, M. H. Crustal and uppermost mantle shear velocity structure adjacent to the Juan de Fuca Ridge from ambient seismic noise. *Geochem. Geophys. Geosyst.* **14**, 3221–3233 (2013).
43. Herrmann, R. B. Computer Programs in Seismology: An evolving tool for instruction and research. *Seismol. Res. Lett.* **84**, 1081–1088 (2013).
44. Hacker, B. R. & Abers, G. A. Subduction Factory 3: An Excel worksheet and macro for calculating the densities, seismic wave speeds, and H₂O contents of minerals and rocks at pressure and temperature. *Geochem. Geophys. Geosyst.* **5**, <https://doi.org/10.1029/2003gc000614> (2004).
45. Brocher, T. M. Empirical relations between elastic wavespeeds and density in the Earth’s crust. *Bullet. Seismol. Soc. Am.* **95**, 2081–2092 (2005).
46. Ruan, Y., Forsyth, D. W. & Bell, S. W. Shear attenuation beneath the Juan de Fuca plate: Implications for mantle flow and dehydration. *Earth Planetary Sci. Lett.* **496**, 189–197 (2018).
47. Turcotte, D. L. & Schubert, G. (2002). *Geodynamics* (pp. 207–208). Cambridge, United Kingdom: Cambridge University Press. <https://doi.org/10.1017/cbo9780511807442>
48. Seton, M. et al. A global data set of present-day oceanic crustal age and seafloor spreading parameters. *Geochem. Geophys. Geosyst.* **21**, <https://doi.org/10.1029/2020gc009214> (2020).

Acknowledgements

We thank all reviewers for insightful comments that helped to improve the quality of this paper. We thank Shane Zhang and Hongda Wang for their contributions in producing the Rayleigh phase speed dataset. We are grateful to Chuanming Liu, Shunjie Han and Tao Yuan for their valuable suggestions. We also thank Joseph Byrnes for sharing the plate age and seismic model with us. Aspects of this research were supported by the National Science Foundation Grant EAR–1537868 at the University of Colorado Boulder. This work utilized the supercomputing cluster Alpine, which is jointly funded by the University of Colorado Boulder, the University of Colorado Anschutz, Colorado State University, and the National Science Foundation (award 2201538).

Author contributions

M.H.R. and M.W. proposed the original idea. M.W. analyzed the dataset and model, made predictions and comparisons. M.W. and M.H.R. wrote and revised the paper.

Competing interests

The authors declare no competing interests.

Additional information

Supplementary information The online version contains supplementary material available at <https://doi.org/10.1038/s43247-023-01072-1>.

Correspondence and requests for materials should be addressed to Mengyu Wu.

Peer review information *Communications Earth & Environment* thanks James Conder and the other, anonymous, reviewer(s) for their contribution to the peer review of this work. Primary Handling Editors: João Duarte and Joe Aslin. A peer review file is available.

Reprints and permission information is available at <http://www.nature.com/reprints>

Publisher’s note Springer Nature remains neutral with regard to jurisdictional claims in published maps and institutional affiliations.



Open Access This article is licensed under a Creative Commons Attribution 4.0 International License, which permits use, sharing, adaptation, distribution and reproduction in any medium or format, as long as you give appropriate credit to the original author(s) and the source, provide a link to the Creative Commons license, and indicate if changes were made. The images or other third party material in this article are included in the article's Creative Commons license, unless indicated otherwise in a credit line to the material. If material is not included in the article's Creative Commons license and your intended use is not permitted by statutory regulation or exceeds the permitted use, you will need to obtain permission directly from the copyright holder. To view a copy of this license, visit <http://creativecommons.org/licenses/by/4.0/>.

© The Author(s) 2023